Journal of Materials Chemistry C

PAPER

View Article Online
View Journal | View Issue

Cite this: J. Mater. Chem. C, 2019, 7, 15074

Aluminium and zinc co-doped $CuInS_2$ QDs for enhanced trion modulation in monolayer WS_2 toward improved electrical properties†

Jian Zhang, *[ab] Bowen Wang,[b] Mike Tebyetekerwa, [b] Yi Zhu,[b] Boqing Liu,[b] Hieu T. Nguyen, [b] Shouqin Tian, *[c] Yupeng Zhang *[a] and Yuerui Lu *[b]

Received 7th October 2019,
Accepted 5th November 2019

DOI: 10.1039/c9tc05469c

rsc.li/materials-c

Considering the significant influence of trions on the optical and electronic properties of two-dimensional transition metal dichalcogenides, the precise tuning of trions in a large range is important for optoelectronic or trion-related applications. Herein, a detailed comparison of eco-friendly $CuInS_2$ (CIS) quantum dots (QDs) and (Al, Zn) co-doped CIS QDs on tuning the trion ratio and electrical properties in a mechanically-exfoliated monolayer (ML) WS_2 is presented. With a similar QD thickness, the trion modulation ability of CIS QDs is largely enhanced after co-doping due to existing extra donor states. In particular, the trion ratio of ML WS_2 can be precisely tuned from 0.05 to 0.7 by varying the QD species and QD thickness, while only a small range (0.05–0.15) of the trion ratio in ML WS_2 is achieved under gate voltage. Moreover, the electron mobility and electron concentration of WS_2-based field-effect transistors (FETs) are significantly improved after QD modification, exhibiting potential applications in FETs and photodetectors.

1. Introduction

Due to quantum confinement and reduced screening, neutral excitons with a higher binding energy can be formed through strongly enhanced electron–hole Coulomb interaction in two-dimensional (2D) layered transition metal dichalcogenides (TMDs).[1] In addition to neutral excitons, charged excitons called trions composed of two electrons and one hole (or two holes and one electron) can be excited due to intentionally or non-intentionally doping, which can also contribute to the emission of 2D TMDs as well as electronic properties.[2] Since the discovery of trions can stably exist in 2D TMDs at room temperature, the study of many-body effects[3] and spin manipulation[4] could be more effective. Moreover, extensive investigations have been reported based on trion formation dynamics,[5,6] binding energy of trions,[7] fundamental valley dynamics,[8] quantum information processing, polarization[9] under a magnetic field or electric field, *etc.*, indicating the important role of trions. Therefore, it is of significant importance to precisely tune the trions of 2D TMDs, and then optimize the optoelectronic device performance. Among the commonly reported four kinds of mechanically exfoliated TMDs (MoS_2, $MoSe_2$, WS_2 and WSe_2), monolayer (ML) WS_2 exhibited the highest PL intensity under the same excitation conditions. However, the trion peak in ML WS_2 cannot be discernible at room temperature, leading to a much lower trion ratio of WS_2 without enough free carriers, which will certainly be an obstacle for its optoelectrical or valleytronic application.

It has been reported that the optical properties of ML TMD can be manipulated through electrostatic doping by using a back-gated field-effect transistor (FET),[10] chemical/physical adsorption of electron-withdrawing/donating surface layers[2,11] or using high frequency sound wave coupling,[12] leading to the changes of the spectral weight between neutral excitons and trions in the photoluminescence spectra of 2D TMDs. For example, the electron concentration of ML MoS_2 was significantly increased after surface functionalization of Cs_2CO_3, leading to an enhanced photocurrent and a quenched PL intensity due to the formation of trions.[13] In addition, the PL properties of ML MoS_2 were enhanced by the adsorption of p-type dopants (F_4TCNQ) and reduced by the adsorption of n-type dopants (NADH), which result from the switch between the exciton and the trion, depending on the carrier density of ML MoS_2.[14] Despite this, it is still challenging to generate and precisely control the trion ratio in a wide range for further valleytronic or spin electronic-related

[a] Key Laboratory of Optoelectronic Devices and Systems of Ministry of Education and Guangdong Province, College of Optoelectronic Engineering, Shenzhen University, Shenzhen 518060, China
[b] Research School of Engineering, College of Engineering and Computer Science, The Australia National University, Canberra, Australian Capital Territory 2601, Australia. E-mail: jian.zhang1@anu.edu.au, yuerui.lu@anu.edu.au
[c] State Key Laboratory of Silicate Materials for Architectures, Wuhan University of Technology, No. 122, Luoshi Road, Wuhan 430070, China

† Electronic supplementary information (ESI) available. See DOI: 10.1039/c9tc05469c

optoelectrical applications. Recently, hybrid nanostructures (0D–2D) composed of semiconducting quantum dots (QDs) and ML TMDs have been considered as a superior hybrid over pristine 2D TMDs when utilized in optoelectronic applications,[15] such as solar photovoltaics,[16] solid-state lighting,[17] and photodetectors.[18] In particular, taking advantage of the strong light absorption and wide absorption range of QDs, 0D–2D QDs-TMDs have been widely reported for photodetector applications,[19] which exhibited largely enhanced photoresponse in a broad-spectrum ranging from the UV-visible to NIR region.[20] However, detailed analysis based on tunability in the optical properties of QD-modified ML TMDs is scarce, except for the PL quenching after incorporating semiconducting QDs due to the charge transfer between the two phases. Moreover, commonly reported QDs are based on heavy-metals, such as PbS QDs, HgTe QDs, CdSe QDs, *etc.*, which will limit their employment in practical applications due to their inherent toxicity.

Ternary colloidal $CuInS_2$ QDs, which offer multiple degrees of freedom for controlling their physical properties *via* stoichiometric alteration,[21,22] have stimulated much research interest in many fields enabled by their solution processability, environmentally friendliness, high PL quantum yields, and size-tunable band gap energies. Moreover, related chemical modification, such as construction of the core–shell structure,[23–25] metal doping,[22,26–28] *etc.*, was also employed to further enhance the optical properties of $CuInS_2$. In particular in our previous work,[29] Zn and Al co-doped $CuInS_2$ QDs exhibited a largely enhanced PL intensity with a redshift emission compared to bare $CuInS_2$, which could be helpful for further optoelectrical applications. Hence, in this work, a detailed comparison of bare $CuInS_2$ QDs and (Al, Zn) co-doped $CuInS_2$ QDs to the optoelectrical properties of ML WS_2, including trion modulation ability, FETs and photodetector properties, was systemically investigated. We show that the tunability (increase rate and range) in the trion ratio and electrical properties of ML WS_2 can be precisely achieved by the QD species and QD thickness, providing a guideline for exploring many potential optoelectrical and valleytronic applications.

2. Experimental section

2.1 Preparation of bare CIS QDs, Al and Zn co-doped CIS QDs

Bare CIS QDs were prepared by mixing 0.4 mmol CuI, 0.4 mmol $In(CH_3COO)_3$, 0.4 mL oleylamine, 2 mL DDT and 2 mL ODE in a three-neck round-bottom flask under an argon atmosphere. And then the mixture was heated to 120 °C with magnetic stirring for 1 h. Afterwards, the reaction mixture was heated to 230 °C for 15 min. Finally, the bare CIS QDs were cooled to room temperature immediately, and then diluted with 20 mL octadecene. (Zn, Al) co-doped CIS QDs were prepared using CIS solution. Firstly, the CIS solution was evacuated for 30 min at 120 °C, and the reaction temperature was maintained at 230 °C under an argon atmosphere. The precursor solution containing $Zn(OA)_2$ and a mixture of 1 mL DDT and 0.25 mmol $Al(IPA)_3$ were continuously injected to the CIS solution through a syringe pump, respectively. After 30 min of reaction, the solution was finally cooled to room temperature and then precipitated with acetone and further dispersed in hexane.

2.2 Device fabrication and measurement

Back-gated FET devices were fabricated using a mechanically-exfoliated monolayer WS_2 sample to investigate the effect of QDs on the optical and electrical properties. The samples were spin-coated with LOR3A at 3000 rpm for 45 s and baked at 180 °C for 5 min. And then the second layer of A2mir 701 was spin-coated on the samples at 6000 rpm for 1 min followed by baking for 5 min at 85 °C. After this, the devices were put into a developing solution for 25 s. A subsequent electron-beam deposition of Ti/Au (5 nm/40 nm) was performed and it was lifted-off in acetone. The devices were annealed in a vacuum tube furnace for 30 min. The obtained FETs were measured at room temperature under atmospheric pressure with a four-probe station equipped with a Keithley semiconductor characterization system. And then two kinds of QDs were spin-coated on the obtained FETs for further electrical measurements.

2.3 Material characterization

The chemical state of CIS QDs and co-doped CIS QDs was examined by X-ray photoelectron spectroscopy (XPS, VG Multilab 2000×, Thermo Fisher Scientific Inc., Waltham, MA). All binding energies of the XPS spectra were referenced to the C 1s peak at 283.8 eV. Transmission electron microscopy of the two kinds of QDs was conducted using a JEM-1010 TEM instrument. The X-ray diffraction (XRD) patterns were obtained using a D/MAX-Rb diffractometer (RIGAKU, Japan). The UV-visible absorption spectrum was obtained using a PerkinElmer 1050 spectrometer with an integrating sphere detector. The as-prepared bare WS_2 and QD-modified WS_2 with different QD thicknesses were characterized by optical microscopy. All the optical path length (OPL) characterizations were performed using a phase-shifting interferometer. PL measurements were conducted using a Horiba LabRAM system equipped with a confocal microscope, a charge-coupled device (CCD) Si detector (detection range between 400–1000 nm), and a 532 nm diode-pumped solid state (DPSS) laser as the excitation source. It should be noted that the on-sample excitation power was always 52 μW, and the acquisition time was 1 s for the room-temperature PL and spatial mapping measurements. The laser light was focused on the sample surface *via* an objective lens. The diameter of the illuminated spot on the samples was about 1.2 μm. The spectral response of the entire system was determined using a calibrated halogen-tungsten light source. For gate-dependent PL measurements, the 100 nm thick gold electrode was transferred to cover part of a single flake as the probing pad. An electrical bias was applied using a Keithley 4200 semiconductor analyzer.

3. Results and discussion

X-ray diffraction (XRD) measurements were firstly performed to investigate the phase structure of the as-prepared bare $CuInS_2$ (CIS) QDs and (Al, Zn) co-doped CIS QDs, as shown in Fig. 1a.

Both of their XRD patterns can be indexed to the tetragonal structure (JCPDS No. 27-0159). It shows well-defined peaks having orientations in the (112), (200), (204), (116), (400), (316), and (424) planes. No detectable differences and no mixed phases were found between these two XRD patterns, which indicated that Al- and Zn-related compounds were not formed. Here, to further illustrate the composition and the chemical state of the elements existing in the as-prepared QDs, the XPS spectra of bare CIS and co-doped CIS were obtained, as shown in Fig. S1 (ESI†). From the XPS survey scans shown in Fig. S1a (ESI†), the expected Cu, In and S peaks without any other impurity peaks are confirmed in bare CIS QDs, and the extra Al and Zn peaks are also confirmed in co-doped CIS QDs. Moreover, the Cu 2p, In 3d and S 2p core levels were also examined. It can be found that the binding energies of Cu $2p_{3/2}$ and Cu $2p_{1/2}$ in the co-doped QDs shift to a lower energy slightly compared to those of the bare CIS QDs, probably arising from different Cu compositions due to Zn and Al doping. Together with the existence of Zn^{2+} and Al^{3+} in co-doped CIS QDs confirmed by the Al 2p and Zn 2p spectra, a similar binding energy shift was also observed in In 3d and S 2p, further indicating that Zn^{2+} and Al^{3+} were indeed incorporated into the CIS QDs. In addition, the fundamental optical characterization of bare CIS QDs and co-doped CIS QDs was also performed to provide the difference in absorption and emission between bare CIS QDs and co-doped CIS QDs. Fig. 1b shows the UV-vis absorption of the as-prepared QDs, and it can be found that the absorption peak of co-doped CIS was clearly red-shifted compared to that of bare CIS QDs. In particular, co-doped QDs exhibited enhanced light adsorption in the visible range, which could be more helpful for the photodetector with enhanced response and an enlarged absorption range. Moreover, as shown in Fig. 1c, due to the reduced surface state and the existence of Al_{Cu} and Zn_{Cu} defects in the middle gap,[29] the co-doped CIS QDs exhibited a largely enhanced PL intensity with a red-shifted wavelength compared to bare CIS QDs, which was consistent with the UV-vis absorption results. Moreover, to further indicate the microstructure and the distribution of the as-prepared QDs, low- and high-magnification transmission electron microscopy (TEM) images were also obtained, as shown in Fig. 1d and e. It can be seen from the low magnification TEM images that the prepared bare CIS and doped CIS showed a uniform size distribution. And the lattice fringes in the high-resolution TEM images show an interplanar distance of 0.32 nm, which can be assigned to the (112) plane of the tetragonally structured CIS. According to the statistical analysis of QD size, the mean size of the CIS QDs and doped CIS is around 4.5 nm and 4 nm, respectively.

To explore the effect of QDs on the optical properties of ML WS_2, we introduce an Au electrode-assisted transfer approach to fabricate ML WS_2 with and without QD modification for a better comparison, as shown in Fig. 2a. The whole fabrication process can be divided into four steps. Firstly, an Au electrode as a mask was transferred on SiO_2/Si substrates. Secondly, QDs (bare or co-doped) with different thicknesses were spin-coated on the substrate with a part of covered Au electrode. Thirdly, the Au electrode was picked up from the substrate, and then an area without QDs can be formed. At last, mechanically exfoliated ML WS_2 was transferred on the interface of the area with and without QDs. According to the above described method, the ML WS_2-CIS heterostructure and the ML WS_2-doped CIS heterostructure were fabricated, as shown in Fig. 2b and c. The clear interface along the white dotted line can be observed between the bare ML WS_2 and the ML WS_2 modified with QDs. Furthermore, the layer number of WS_2 and the relative thickness of QDs were also confirmed by using a reported technique phase-shifting interferometry, depending on the contrast under an optical microscope.[30] The optical path length (OPL) of the black

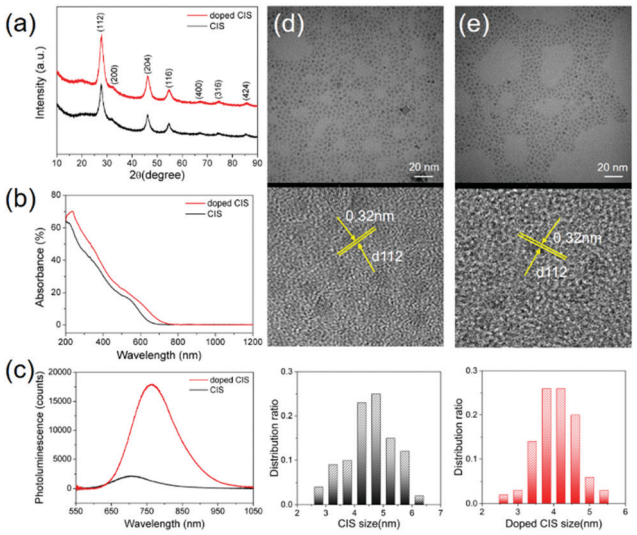

Fig. 1 (a) XRD patterns of bare CIS and doped CIS; (b) UV-visible absorption spectra of bare CIS and co-doped CIS. (c) Room-temperature PL spectra of bare CIS and co-doped CIS based on thicker layer QDs. (d) Low- and high-magnification TEM images, and the corresponding size statistical analysis result of bare CIS and (e) Low- and high-magnification TEM images of co-doped CIS, and the corresponding size statistical analysis result of co-doped CIS.

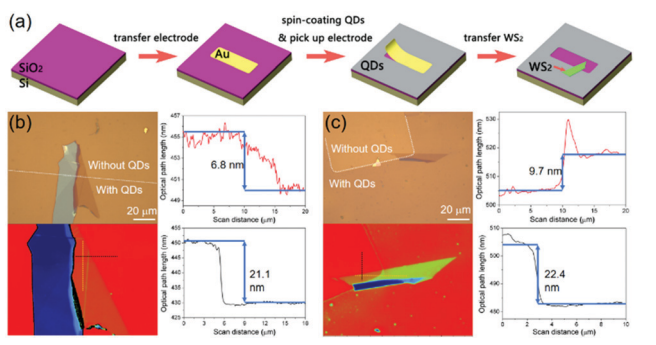

Fig. 2 (a) Process flow diagram of monolayer WS_2 with and without QD modification for a better comparison. (b) Optical image of WS_2-CIS and the corresponding PSI measured optical path length (OPL) values of WS_2 and CIS along the black dotted line and the red dotted line, respectively. (c) Optical images of WS_2-doped CIS and the corresponding PSI measured OPL values of WS_2 and doped CIS along the black dotted line and the red dotted line, respectively. Note: the white dotted line in two figures stands for the interface with and without QDs.

and red lines across the transferred WS_2 nanosheets stands for the thickness of WS_2 and QDs, respectively. The OPLs of 21.1 nm and 22.4 nm for the bare WS_2 indicate the monolayer characteristic of transferred WS_2,[30–32] whereas OPLs of 6.8 nm and 9.7 nm across the interface are the relative thickness of CIS and co-doped CIS, respectively. Additionally, to analyze the dispersion of CIS QDs and co-doped CIS QDs, chips with two kinds of QDs were prepared for PL intensity mapping tests. For a better comparison, a Au-assisted method was also adopted to form two regions with QDs and without QDs, as shown in Fig. S2 (ESI†). It can be found that the PL intensity of co-doped QDs is higher than that of bare CIS QDs, which is consistent with the former results in Fig. 1c. More importantly, the PL intensity of QDs is nearly equal to each other in the coverage area of QDs, both exhibiting a uniform dispersion.

Fig. 3a shows the room-temperature photoluminescence (PL) spectra of bare WS_2 and WS_2-CIS based on the fabricated chip with 6.8 nm CIS QD thickness in Fig. 2b. It can be found that the intensity of the PL emission peak in WS_2-CIS is reduced compared to that in bare ML WS_2, probably due to electron transfer from the donor CIS QDs to the acceptor ML WS_2. To further understand the spectral changes of WS_2 after CIS QD modification, we consider the contributions of the exciton and the trion. Using Lorentzian fitting, the main peak can be decomposed into the exciton peak and the trion peak. It can be observed from Fig. 3a that the trion peak is almost non-discernible in bare ML WS_2, whereas the obvious trion peak can be found in CIS modified WS_2. As for WS_2-doped CIS with 9.7 nm co-doped CIS QD thickness in Fig. 2c, the total PL intensity is dramatically reduced compared to that in the bare ML WS_2, and the intensity of the trion peak is even comparable to that of the exciton peak, as shown in Fig. 3c. Here, to better clarify the different trion modulation ability of CIS and doped CIS, the trion ratio (Tr) can be expressed as follows:

$$\mathrm{Tr} = I_{\mathrm{trion}}/(I_{\mathrm{exciton}} + I_{\mathrm{trion}}) \quad (1)$$

where I_{exciton} and I_{trion} stand for the PL intensity of the exciton peak and the trion peak, respectively. Moreover, the trion increase rate (R_{Tr}) between bare WS_2 and QD modified WS_2 can be defined as:

$$R_{\mathrm{Tr}} = (\mathrm{Tr}_{\mathrm{hetero}} - \mathrm{Tr}_{\mathrm{WS_2}})/\mathrm{Tr}_{\mathrm{WS_2}} \quad (2)$$

where $\mathrm{Tr}_{\mathrm{hetero}}$ and $\mathrm{Tr}_{\mathrm{WS_2}}$ are the trion ratio of WS_2-QDs and bare WS_2, respectively. Therefore, the trion ratio of bare WS_2 and the heterostructure as well as the trion increase rate can be calculated based on the above equations. On the basis of the Lorentzian fitting results, the trion ratios of bare WS_2 and WS_2-CIS are 0.056 and 0.100, whereas the trion ratios of bare WS_2 and WS_2-doped CIS are 0.050 and 0.222, respectively. According to the further calculation, the trion increase rate of WS_2-doped CIS (3.419) is much higher than that of WS_2-CIS (0.788). It should be noted that the emission peak intensities of CIS and doped CIS QDs cannot be observed in these two chips, probably due to the relatively weak PL intensity of QDs with less thickness compared to ML WS_2 under the same excitation conditions. Here, to explore the effect of QD thickness on the PL intensity of QDs and the trion modulation in ML WS_2, ML WS_2 with a series of different CIS and doped CIS thicknesses was successfully prepared by tuning the number of spin-coating, and the corresponding optical images, the OPL results and the PL spectra are shown in Fig. S3 and S4 (ESI†). As for the fabricated WS_2-CIS chip with different CIS thicknesses, the trion increase rate is changed from 0.453 to 2.327 when the CIS QD thickness is in the range of 2.3 nm to 12.7 nm (Fig. 3b). The trion increase rate for WS_2-doped CIS is also increased from 1.174 to 5.462 when the doped-CIS QD thickness is in the range of 6.6 nm to 24.9 nm (Fig. 3d). It should be mentioned that the OPL values of QDs (from 2.3 nm to 24.9 nm) are not the actual thickness of QD thin films, which are only used to provide the changes in the QD thickness. For a better understanding, the AFM images of QD thin films with the lowest thickness and the highest thickness are also given, as shown in Fig. S3 and S4 (ESI†). It was found that the OPL value of 2.3 nm in the first CIS QD thin film corresponds to the 4.18 nm actual CIS thickness, and the OPL value of 24.9 nm in the fifth doped-CIS thin film corresponds to the 13.1 nm actual doped-CIS thickness. Additionally, the 0.73 nm and 0.85 nm actual thickness of bare WS_2 further indicates the monolayer characteristic of WS_2. Obviously, the trion increase rate in WS_2-doped CIS is much higher than that of WS_2-CIS in the whole range of QD thicknesses, implying the higher trion modulation ability of doped

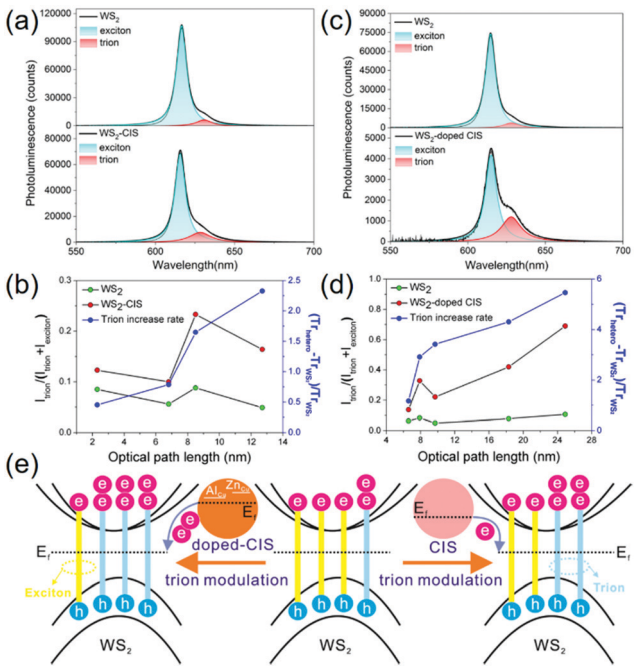

Fig. 3 (a) Room-temperature PL spectra of bare ML WS_2 and WS_2-CIS; the fitted cyan area and red area represent the exciton and the trion, respectively. (b) Comparison of the trion ratio and the trion increase rate in bare ML WS_2 and WS_2-CIS at different CIS thicknesses. (c) Room-temperature PL spectra of bare ML WS_2 and WS_2-doped CIS; the fitted cyan area and red area represent the exciton and the trion, respectively. (d) Comparison of the trion ratio and the trion increase rate in bare ML WS_2 and WS_2-doped CIS at different doped CIS thicknesses. (e) Schematic diagrams of trion modulation in ML WS_2 after QD modification.

CIS. It should be noted that the PL emission peak at 750 nm that belong to doped CIS appears only when the QD thickness reach 24.9 nm due to the relatively weak PL intensity of QDs compared to ML WS_2, as shown in Fig. S4 (ESI†). Based on the fabricated chip with 24.9 nm co-doped CIS QD thickness, low temperature PL spectra of bare WS_2 and WS_2-doped CIS are also shown in Fig. S5 (ESI†). It can be found that the trion peak in WS_2 and WS_2-doped CIS become more and more prominent upon decreasing the temperature, because the kinetic energy of the neural exciton increases by thermal activation and results in a decrease of the trion formation rate when temperature increases.[33] Similarly, the trion ratio of WS_2-doped CIS is still higher than that of bare WS_2 at low temperature. Interestingly, the exciton peak disappeared upon further decreasing the temperature, and only the trion peak can be observed in WS_2-doped CIS while a relatively higher PL emission intensity can also be ensured, which could be more helpful for the trion-based valleytronic application at low temperatures. Moreover, to better detail the effect of QDs on the optical properties of bare ML WS_2, the schematic diagram is also given, as shown in Fig. 3e. The trion modulation ability of these two kinds of QDs can be explained by the electron-doping effect, which means excess electrons induced by QD modification can effectively bind with photoexcited electron–hole pairs and then form negative trions in WS_2. Also, the higher trion modulation ability of doped CIS reveals that the number of electrons transferred to ML WS_2 is larger than that of CIS due to the existence of donor states, such as Al_{Cu}, Zn_{Cu}, and then the switch between excitons and negative trions can be more facile. Additionally, because the effective charge transfer usually occurs across the interface, the persistent trend of the increasing trion ratio will not occur with further increase in the QD thickness. Therefore, we can obtain a conclusion that the trion ratio of monolayer WS_2 can be well-tuned from 0.05 to 0.7 by varying the QD species and QD thickness.

To confirm the electron-doping effect of CIS and doped-CIS QDs, the gate-dependent PL spectra of WS_2 modified with CIS and doped CIS were also employed. The device structure and the corresponding PL spectra of bare WS_2 and the heterostructure are shown in Fig. S6 and S7 (ESI†). It should be pointed out that the top-gate voltage was directly applied to ML WS_2 through a Au contact pad, and the Si substrate was electrically grounded using copper conductive adhesive. As for the fabricated WS_2-CIS chip in Fig. 4a, the trion ratio of bare WS_2 increased under a negative gate voltage and decreased under a positive gate voltage. Under positive gate voltage, the injected holes will neutralize the electrons in WS_2, and then the negatively trion was transferred to the exciton, thus decreasing the trion ratio. Under negative gate voltage, the injected electrons will continue to bond photoexcited electron–hole pairs to form a larger number of trions. Therefore, the increased trion ratio of WS_2-CIS and WS_2-doped CIS described in Fig. 3 is equal to the effect of imposing a negative gate voltage on ML WS_2, indicating the electron-doping effect of CIS and doped CIS. Besides, it was found that the trion ratio of WS_2-CIS is higher than that of bare WS_2 under the same gate voltage in the range of negative 30 V to positive 30 V, and the trion ratio of WS_2-CIS under zero gate voltage is even higher than that of bare WS_2 under negative 30 V,

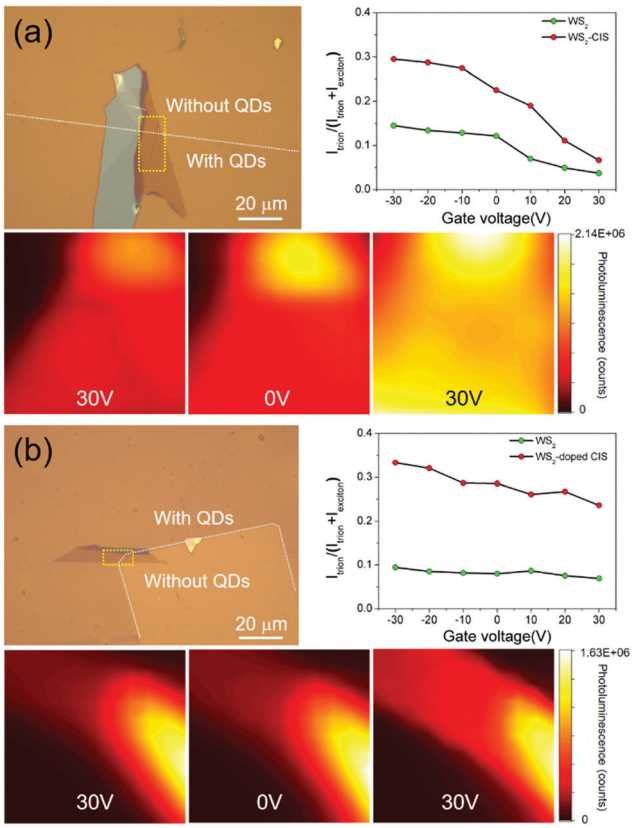

Fig. 4 (a) The optical image of the fabricated WS_2-CIS chip, the white dotted line indicates the interface with and without CIS QDs, and the yellow area indicates the mapping area; comparison of the trion ratio in bare ML WS_2 and WS_2-CIS under different gate voltages; the PL intensity mapping under −30 V, 0 V and 30 V based on the yellow area. (b) The optical image of the fabricated WS_2-doped CIS chip, the white dotted line indicates the interface with and without doped-CIS QDs, and the yellow area stands for the mapping area; comparison of the trion ratio in bare ML WS_2 and WS_2-doped CIS under different gate voltages; the PL intensity mapping under −30 V, 0 V and 30 V based on the yellow area.

which indicates that the trion modulation ability of CIS QD modification is much higher than that of gate voltage, implying the important role of QD modification. For a better comparison, gate-dependent PL measurements based on WS_2-doped CIS were also carried out, and the corresponding trion ratio was extracted in Fig. 4b. A similar change trend of the trion ratio can also be observed under different gate voltages. Although the trion ratios of WS_2-CIS and WS_2-doped CIS are all around 0.3 under different gate voltages, the gap between the trion ratio of WS_2-doped CIS and the trion ratio of bare WS_2 is much larger than that of the fabricated WS_2-CIS chip, which indicates the higher trion increase rate (R_{Tr}) of WS_2-doped CIS. Therefore, we can draw the conclusion that doped CIS QDs exhibit enhanced trion modulation ability, which is consistent with the former described results in Fig. 3. More obviously, as for the fabricated WS_2-doped CIS chip, the trion ratios of bare WS_2 and WS_2-doped CIS were almost unchanged under different gate voltages, whereas the trion ratio of WS_2 was largely enhanced by doped CIS modification, further indicating the important role of co-doped QDs in trion modulation. Here, the PL mapping

images of WS_2-CIS and WS_2-doped CIS under negative 30 V, 0 V and 30 V were also obtained to better clarify the changes in the PL intensity. Indeed, the formation of trions will lead to the reduction of the PL intensity as the non-radiative recombination channels are dominating for trions.[34] Hence, negative gate voltage-induced trions lead to a decreased PL intensity in the WS_2 area and the heterostructure area, whereas an enhanced PL intensity can be observed under positive gate voltage due to the reduced number of trions, which are in accordance with the spectra results in Fig. S6 and S7 (ESI†). Due to the large number of trions, the WS_2-CIS and WS_2-doped CIS exhibited a much lower PL intensity compared to bare WS_2 under zero gate voltage. Interestingly, the PL intensities of the heterostructure area under positive voltage in these two chips are even comparable to that of bare WS_2, while the PL intensity of WS_2 was almost unchanged by the tuning gate voltage, which means that excess electrons induced by QD modification offer more space for gate-voltage regulation. In this circumstance, the trion ratio of bare WS_2 can be precisely tuned in a large range through doped-CIS QD modification for further optoelectrical and valleytronic applications; meanwhile, the comparable PL emission intensity can also be ensured by imposing a suitable gate voltage.

Moreover, to evaluate the effect of CIS QDs and co-doped CIS QDs on the electronic properties of ML WS_2, back-gated field-effect transistor (FET) devices based on bare WS_2, WS_2-CIS and WS_2-doped CIS with two different thicknesses were fabricated by a photolithography method and subsequently by e-beam evaporation, and the corresponding optical images of the FET chips are shown in Fig. S8 (ESI†). Fig. 5a shows source–drain current as a function of gate voltage (V_g–I_{ds}) curves of as-prepared four chips under a drain voltage of 3 V, all exhibiting a typical n-type behaviour. It can be also found that the I_{ds} of WS_2 slightly increased with increasing V_g, while the I_{ds} of WS_2 after QD modification largely increased compared to that of bare WS_2, especially for co-doped CIS QD modified samples. Moreover, the increased rate of I_{ds} is further enlarged by increasing the QD thickness. The enhanced current can be explained by the increase in the electron concentration after QD modification. Besides, the threshold voltage (V_{th}) shifts toward the negative voltage after QD modification, indicating the electron-doping effect of CIS QDs and co-doped CIS QDs. To further prove the electron-doping effect of CIS QDs and doped-CIS QDs, the electron mobility and electron concentration were also estimated based on Fig. 5a. The field-effect mobility (μ) can be extracted based on the linear region of the transfer curves using the following equation:[35]

$$\mu = (L/W) \times (dI_{ds}/dV_g) \times (1/V_{ds}) \times (d/\varepsilon_0\varepsilon_r) \quad (3)$$

where L and W are the channel length and width, dI_{ds}/dV_g is the slope of the transfer characteristics of an FET device, V_{ds} is the drain voltage, ε_0 and ε_r are the vacuum permittivity and relative permittivity of SiO_2, respectively, and d is the thickness of SiO_2. Besides, the electron concentration (n) can be obtained from the calculated electron mobility as follows:[13]

$$n = 1/\mu\rho q \quad (4)$$

where ρ is the resistivity of the channel. Therefore, the electron mobility and electron concentration of the as-fabricated FET chips can be calculated by using eqn (3) and (4), as shown in Fig. 5b. The electron-doping effect of QDs was further confirmed by the increased electron concentration in CIS QD modified WS_2 at V_g = 0 V, and the electron concentration of WS_2-doped CIS is higher than that of WS_2-CIS, indicating the higher electron-doping ability of co-doped CIS QDs. Considering the different electron concentrations of WS_2-doped QDs with different QDs thicknesses, we can draw a conclusion that the electron-doping ability can also be tuned by changing the QD thickness except for two element co-doping. Moreover, through modifying QDs and tuning QD thickness, the field-effect mobility was also enhanced compared to that of bare ML WS_2, probably arising from the reduced surface scattering effect after QD modification. Besides, the IV curves of the fabricated chips with and without light irradiation at V_g = 10 V are also shown in Fig. 5c and d, and the I_{ds} of the as-fabricated chips under light illumination (380–780 nm, 15 mW) increased compared with that in the dark state. Herein, we can define the photocurrent as the V_{ds} difference with and without light irradiation. It can be found that the gaps between the light and dark state of bare WS_2, WS_2-CIS, WS_2-doped CIS1 and WS_2-doped CIS2 are 0.20 nA, 0.63 nA, 4.41 nA and 40.09 nA, respectively, indicating that the photocurrent of WS_2 is largely enhanced by QD modification. The largely enhanced photocurrent could be attributed to the electron-doping induced trions that can significantly reduce the recombination of photoexcited electron–hole pairs, which is consistent with the above described optical properties in QD modified ML WS_2. Similarly, except for the higher electron concentration of WS_2-doped CIS, the photocurrent increase rate of the doped CIS QD-based FET chip is also higher than that of the CIS QD-based FET chip, further indicating the higher electron-doping ability of co-doped QDs. Therefore, together with the described red-shift of the absorption peak in co-doped CIS QDs (Fig. 1b), it can be expected that co-doped CIS QDs as a kind of surface modifier can

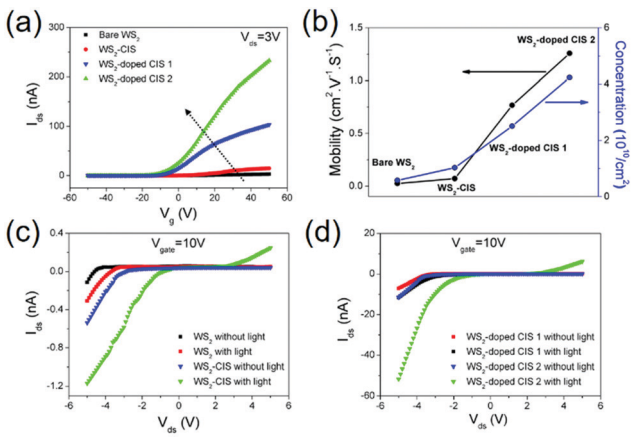

Fig. 5 (a) Transfer characteristics of the bare ML WS_2, WS_2-CIS and WS_2-doped CIS with two different thicknesses (V_{ds} = 3 V). (b) Estimated field-effect mobility, and electron concentration of as-fabricated four chips at V_g = 0 V. (c) IV curves of bare WS_2 and WS_2-CIS at V_g = 10 V without and with light. (d) IV curves of WS_2-doped CIS with two different thicknesses at V_g = 10 V without and with light.

enhance the sensitivity of ML WS_2-based photodetectors with broadband response.

4. Conclusions

To conclude, we have demonstrated the effect of $CuInS_2$ (CIS) quantum dots (QDs) and (Al, Zn) co-doped CIS QDs on the optical properties and electronic properties of monolayer WS_2, and tunable optical and electrical properties are achieved by changing the type and the thickness of QDs. As compared with the bare monolayer WS_2, the PL intensities of WS_2 decrease after QD modification. The further PL spectra fittings show that the PL spectrum of monolayer WS_2 after QD modification is dominated by the trion peak, leading to an increased trion ratio in QDs-WS_2 compared to bare WS_2. On the basis of the definition of the trion ratio and the trion increase rate, it can be found that the trion ratios of WS_2-doped CIS and WS_2-CIS increased with increasing QD thickness, and the trion increase rate of WS_2-doped CIS is much higher than that of WS_2-CIS with a similar QD thickness, indicating that the trion ratio of bare ML WS_2 can be precisely tuned in a large range by changing the QD species and the QD thickness. A similar increased trion ratio in gate-dependent PL from positive to negative voltage indicates the electron-doping effect of QD modification. Moreover, the important role of QDs in trion modulation is further validated by comparing a little change in the gate-voltage-induced trion ratio with the largely enhanced trion ratio in QD-modified ML WS_2. Additionally, although the PL intensity of ML WS_2 was largely decreased by QD modification, the PL intensity of QD-modified ML WS_2 under 30 V top-gate voltage is even comparable to that of bare ML WS_2, endowing QD-modified ML WS_2 with a higher trion ratio for valleytronic application without sacrificing the PL emission intensity. In addition to the optical property modification, the effect of two kinds of QDs on the electrical properties of bare ML WS_2 is also detailed. The I_{ds}–V_g curves revealed that the threshold voltage (V_{th}) is shifted in the negative direction after QD modification, further indicating the electron-doping effect of two kinds of QDs. And the calculated electron mobility and electron concentration in WS_2-doped CIS are higher than those of bare WS_2 and WS_2-CIS, and this enhancement was further enlarged by increasing the doped-CIS QD thickness. Besides, the largely enhanced photocurrent of WS_2 after QD modification was also observed, which could be used as a kind of potential photodetector. Our work demonstrates the tunability of the trion ratio, FET properties and photocurrent, which is very important for exploiting the TMDs for further valleytronic and electronic applications.

Conflicts of interest

There are no conflicts to declare.

Acknowledgements

The authors thank the ACT node of the Australian National Fabrication Facility (ANFF). The authors also thank the National Natural Science Foundation of China (51802104).

Notes and references

1 C. H. Lui, A. J. Frenzel, D. V. Pilon, Y. H. Lee, X. Ling, G. M. Akselrod, J. Kong and N. Gedik, *Phys. Rev. Lett.*, 2014, **113**, 166801.
2 F. Cadiz, S. Tricard, M. Gay, D. Lagarde, G. Wang, C. Robert, P. Renucci, B. Urbaszek and X. Marie, *Appl. Phys. Lett.*, 2016, **108**, 251106.
3 J. Shang, X. Shen, C. Cong, N. Peimyoo, B. Cao, M. Eginligil and T. Yu, *ACS Nano*, 2015, **9**, 647–655.
4 M. Druppel, T. Deilmann, P. Kruger and M. Rohlfing, *Nat. Commun.*, 2017, **8**, 2117.
5 A. Singh, G. Moody, K. Tran, M. E. Scott, V. Overbeck, G. Berghäuser, J. Schaibley, E. J. Seifert, D. Pleskot, N. M. Gabor, J. Yan, D. G. Mandrus, M. Richter, E. Malic, X. Xu and X. Li, *Phys. Rev. B: Condens. Matter Mater. Phys.*, 2016, **93**, 041401.
6 T. Godde, D. Schmidt, J. Schmutzler, M. Aßmann, J. Debus, F. Withers, E. M. Alexeev, O. Del Pozo-Zamudio, O. V. Skrypka, K. S. Novoselov, M. Bayer and A. I. Tartakovskii, *Phys. Rev. B: Condens. Matter Mater. Phys.*, 2016, **94**, 165301.
7 Z. B. Matthew, C. Frank, H.-Y. Chiu and H. Zhao, *ACS Nano*, 2015, **9**, 6459–6464.
8 F. Gao, Y. Gong, M. Titze, R. Almeida, P. M. Ajayan and H. Li, *Phys. Rev. B: Condens. Matter Mater. Phys.*, 2016, **94**, 245413.
9 H. Zeng, J. Dai, W. Yao, D. Xiao and X. Cui, *Nat. Nanotechnol.*, 2012, **7**, 490–493.
10 J. S. Ross, S. Wu, H. Yu, N. J. Ghimire, A. M. Jones, G. Aivazian, J. Yan, D. G. Mandrus, D. Xiao, W. Yao and X. Xu, *Nat. Commun.*, 2013, **4**, 1474.
11 N. Peimyoo, W. Yang, J. Shang, X. Shen, Y. Wang and T. Yu, *ACS Nano*, 2014, **8**, 11320–11329.
12 A. R. Rezk, B. Carey, A. F. Chrimes, D. W. Lau, B. C. Gibson, C. Zheng, M. S. Fuhrer, L. Y. Yeo and K. Kalantar-Zadeh, *Nano Lett.*, 2016, **16**, 849–855.
13 J. Lin, C. Han, F. Wang, R. Wang, D. Xiang, S. Qin, X. Zhang, L. Wang, H. Zhang, A. Wee and W. Chen, *ACS Nano*, 2014, **8**, 5323–5329.
14 S. Mouri, Y. Miyauchi and K. Matsuda, *Nano Lett.*, 2013, **13**, 5944–5948.
15 J. Cheng, C. Wang, X. Zou and L. Liao, *Adv. Opt. Mater.*, 2019, **7**, 1800441.
16 S. Kim, M. Kang, S. Kim, J.-H. Heo, J. Noh, S. Im, S. Seok and S.-W. Kim, *ACS Nano*, 2013, **7**, 4756–4763.
17 D. Prasai, A. R. Klots, A. K. Newaz, J. S. Niezgoda, N. J. Orfield, C. A. Escobar, A. Wynn, A. Efimov, G. K. Jennings, S. J. Rosenthal and K. I. Bolotin, *Nano Lett.*, 2015, **15**, 4374–4380.
18 H. Wu, H. Si, Z. Zhang, Z. Kang, P. Wu, L. Zhou, S. Zhang, Z. Zhang, Q. Liao and Y. Zhang, *Adv. Sci.*, 2018, **5**, 1801219.
19 C. Hu, D. Dong, X. Yang, K. Qiao, D. Yang, H. Deng, S. Yuan, J. Khan, Y. Lan, H. Song and J. Tang, *Adv. Funct. Mater.*, 2017, **27**, 1603605.
20 H. Lu, G. M. Carroll, N. R. Neale and M. C. Beard, *ACS Nano*, 2019, **13**, 939–953.
21 D. H. Jara, K. G. Stamplecoskie and P. V. Kamat, *J. Phys. Chem. Lett.*, 2016, **7**, 1452–1459.

22 K. E. Hughes, S. R. Ostheller, H. D. Nelson and D. R. Gamelin, *Nano Lett.*, 2019, **19**, 1318–1325.
23 K.-T. Kuo, D.-M. Liu, S.-Y. Chen and C.-C. Lin, *J. Mater. Chem.*, 2009, **19**, 6780–6788.
24 P. H. Chuang, C. C. Lin and R. S. Liu, *ACS Appl. Mater. Interfaces*, 2014, **6**, 15379–15387.
25 X. Wang, Z. Liang, X. Xu, N. Wang, J. Fang, J. Wang and G. Xu, *J. Alloys Compd.*, 2015, **640**, 134–140.
26 X. Yuan, R. Ma, W. Zhang, J. Hua, X. Meng, X. Zhong, J. Zhang, J. Zhao and H. Li, *ACS Appl. Mater. Interfaces*, 2015, **7**, 8659–8666.
27 H. J. Yun, J. Lim, A. S. Fuhr, N. S. Makarov, S. Keene, M. Law, J. M. Pietryga and V. I. Klimov, *ACS Nano*, 2018, **12**, 12587–12596.
28 S.-Y. Yoon, J.-H. Kim, E.-P. Jang, S.-H. Lee, D.-Y. Jo, Y. Kim, Y. R. Do and H. Yang, *Chem. Mater.*, 2019, **31**, 2627–2634.
29 M. Zhu, Y. Li, S. Tian, Y. Xie, X. Zhao and X. Gong, *J. Colloid Interface Sci.*, 2019, **534**, 509–517.
30 R. Xu, S. Zhang, F. Wang, J. Yang, Z. Wang, J. Pei, Y. W. Myint, B. Xing, Z. Yu, L. Fu, Q. Qin and Y. Lu, *ACS Nano*, 2016, **10**, 2046–2053.
31 R. Xu, J. Yang, Y. Zhu, H. Yan, J. Pei, Y. W. Myint, S. Zhang and Y. Lu, *Nanoscale*, 2016, **8**, 129–135.
32 J. Yang, R. Xu, J. Pei, Y. W. Myint, F. Wang, Z. Wang, S. Zhang, Z. Yu and Y. Lu, *Light: Sci. Appl.*, 2015, **4**, e312.
33 T. Kato and T. Kaneko, *ACS Nano*, 2016, **10**, 9687–9694.
34 D.-H. Lien, S. Z. Uddin, M. Yeh, M. Amani, H. Kim, J. W. Ager III, E. Yablonovitch and A. Javey, *Science*, 2019, **364**, 468–471.
35 Y. Yue, J. Chen, Y. Zhang, S. Ding, F. Zhao, Y. Wang, D. Zhang, R. Li, H. Dong, W. Hu, Y. Feng and W. Feng, *ACS Appl. Mater. Interfaces*, 2018, **10**, 22435–22444.